Article submitted to: High Power Laser Science and Engineering, 2024 *February 16, 2024*

High-repetition-rate source of nanosecond duration kA-current pulses driven by relativistic laser pulses

Michael Ehret[1], Jakub Cikhardt[2], Philip Bradford[3], Iuliana-Mariana Vladisavlevici[1], Tomas Burian[4], Diego de Luis[1], Jose Luis Henares[1], Rubén Hernández Martín[1], Jon Imanol Apiñaniz[1], Roberto Lera[1], José Antonio Pérez-Hernández[1], João Jorge Santos[3], and Giancarlo Gatti[1]

[1]*Centro de Láseres Pulsados (CLPU), Villamayor, Spain*
[2]*Czech Technical University in Prague, Faculty of Electrical Engineering, Prague, Czech Republic*
[3]*Univ. Bordeaux-CNRS-CEA, Centre Lasers Intenses et Applications (CELIA), UMR 5107, Talence, France*
[4]*Department of Radiation and Chemical Physics, FZU-Institute of Physics of the Czech Academy of Sciences, Prague, Czech Republic*

Abstract

We report the first high-repetition rate generation and simultaneous characterization of nanosecond-scale return currents of kA-magnitude issued by the polarization of a target irradiated with a PW-class high-repetition-rate Ti:Sa laser system at relativistic intensities. We present experimental results obtained with the VEGA-3 laser at intensities from $5 \times 10^{18}\,\mathrm{W\,cm^{-2}}$ to $1.3 \times 10^{20}\,\mathrm{W\,cm^{-2}}$. A non-invasive inductive return-current monitor is adopted to measure the derivative of return-currents on the order of $\mathrm{kA\,ns^{-1}}$ and analysis methodology is developed to derive return-currents. We compare the current for copper, aluminium and Kapton targets at different laser energies. The data shows the stable production of current peaks and clear prospects for the tailoring of the pulse shape, promising for future applications in high energy density science, e.g. electromagnetic interference stress tests, high-voltage pulse response measurements, and charged particle beam lensing. We compare the target discharge of the order of hundreds of nC with theoretical predictions and a good agreement is found.

Keywords: current pulses; electromagnetic pulse application; high power laser; relativistic laser plasma

1. Introduction

The continuous technical and scientific improvement of lasers[1,2] has led to stable short-pulse PW-class high repetition rate Ti:Sa systems[3,4]. If these lasers are tightly focused onto matter, the relativistic interaction yields forward-acceleration of electrons[5] that in turn can trigger pulsed bright ion beams by well known mechanisms such as Target Normal Sheath Acceleration (TNSA)[6,7], Radiation Pressure Acceleration (RPA)[8] and others[9] beneficial to isotope production[10], positron emission tomography[11], ion beam microscopy[12], Particle-Induced X-ray Emission (PIXE)[13] as well as inertial confinement fusion[14]. The mechanisms rely on the build up of large accelerating potentials which are also the source of ultra-strong electromagnetic pulses[15]. In particular, targets attain a strong positive net-charge due to laser-accelerated electrons that are able to escape the rising potential barrier[16]. As a result of this, kA-level discharge pulses and return currents can be produced and propagate over the target surface[17]. Interest in these effects is twofold: (i) both are sensitive to the total amount of charge that leaves the target and therefore can be used as a passive diagnostic of the laser-target interaction; and (ii) both allow to deliver all-optically generated kA-level ns-duration current pulses that can be understood as a novel secondary source.

Note that ns-duration current pulses can also be generated by non-relativistic ns-duration laser pulses of high energy in the wide range of several A up to the MA-level[22–24]. Here, the long laser pulses are issued in the single-shot regime and interact with tailor-made single-shot targets, building up a charge separation that triggers a return current to rise.

The monitoring of target discharge is an important aspect of ultrahigh intensity laser-solid interaction at high-repetition-rate. This paper presents an inductive current monitor as metrology for high-voltage pulses driven at high-repetition-rate. The measurement of return currents with inductive current monitors has been demonstrated previously in the regime of ns-driver lasers with intensities $1 \times 10^{14}\,\mathrm{W\,cm^{-2}}$ to $1 \times 10^{16}\,\mathrm{W\,cm^{-2}}$[33]. We apply this technique to the characterization of discharge pulses driven

Correspondence to: C Adaja 8, ES-37185, or Email: mehret@clpu.es

10.1017/hpl.2024.14

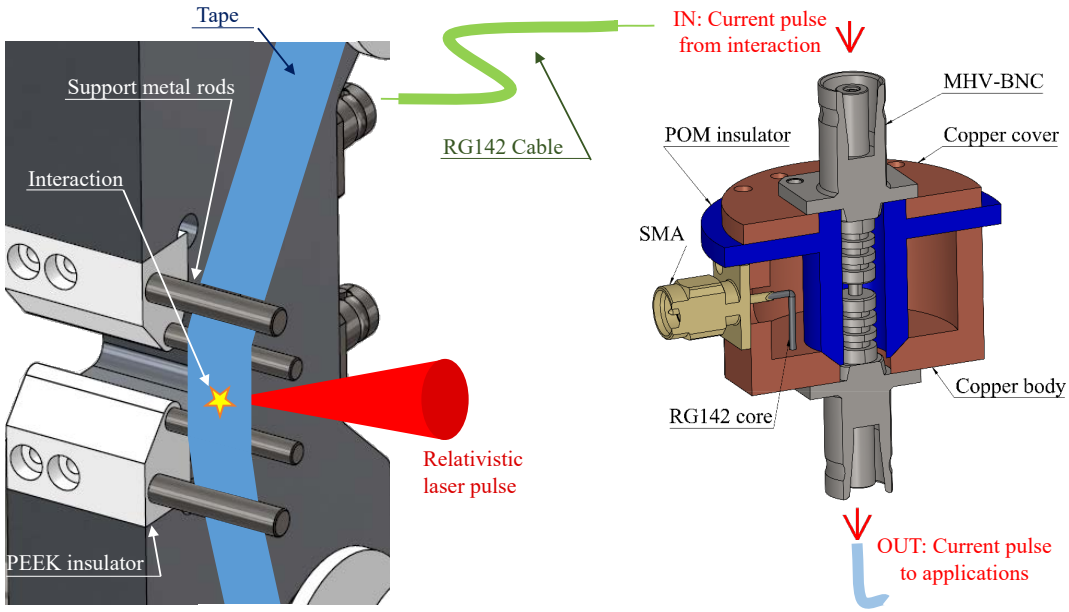

Figure 1. Tape target system (left) and cut of the Target Charging Monitor (right). The Target Charging Monitor (TCM) has two opposite MHV-BNC connectors with soldered pins to pass through the pulsed current issued by relativistic laser interaction in the top to the application side in the bottom. The TCM comprises a solid copper body forming a cup; with a cylindrical top; both later of which are separated by dielectric material POM. The through current induces a magnetic field enclosed in the cylinder which causes an induced current to flow in a small squared loop formed by the core of a RG142 coaxial cable connected to an output SMA connector. The current pulse itself is issued by the discharge of the solid tape target and coupled into one of the insulated support rods of the tape which are connected to a RG142 coaxial cable leading to the TCM via an MHV-BNC connector on the system's chassis. The other support rod is isolated from the ground.

by high power Ti:Sa systems at relativistic intensities.

Pulses of kA-level at ns-duration pose a risk for electronic systems in the vicinity of the interaction[18,19], but they also have an application in the context of proton beam focusing[20,21] and transient magnetic field generation[17]. We demonstrate here for the first time the stable generation of discharge pulses, with a clear perspective to obtain a novel high-repetition-rate source of kA-scale current pulses for future applications, , e.g. on the field of electromagnetic compatibility (EMC) tests[25], radio-location[26], military technologies[27], biology[28], and medicine[29].

2. Materials and Methods

The primary diagnostic used in this study was a Target Charging Monitor (TCM) constructed based on the principles of an inductive current monitor[33]. The TCM measures the derivative of the current that streams through the device as shown in Fig. 1. Key advantage of this metrology technique is its destruction-free nature. Current pulses are excited by laser-plasma interaction on a solid density target, transported through the TCM and can be applied after their characterization.

Current pulses that pass through the TCM device induce a magnetic field inside the cylindrical copper body which causes an induced current to flow in a coil-shaped rod connected to an coaxial output. The calibration factor which relates the time-integrated voltage to the current is $-2.0(3) \times 10^9\,\mathrm{A\,V^{-1}}$ (see Appx. A) [1]. For this work, current pulses are transported via RG142 coaxial cables and the circuit impedance is $Z = 50\,\Omega$. The through signal is terminated in the facility grounding. Note that cable lengths are measured with 3 ns FWHM voltage pulses: target and TCM are connected with a coaxial cable of $9.6(2)$ ns length; and TCM and grounding are connected with a coaxial cable of $13.6(1)$ ns length. Induced signals are transported to a 2 GHz oscilloscope and acquisitions are throughout corrected for the frequency dependent attenuation of circuit elements. Circuit calibrations are done using a R&S ZNH 4 GHz vector network analyzer. The effective bandwidth of the circuit is 2 GHz.

Experiments for this work are conducted at the VEGA-3 laser facility at CLPU with high-power Ti:Sa laser pulses amplified to an energy E_L up to 25 J per pulse measured behind the compressor. After compression to a duration τ_L of 30 fs, the short laser pulse is transported in high-vacuum of 1×10^{-6} mbar via a $f = 2.5$ m off-axis parabola onto the target with a beam-transport efficiency of 82 %. The focal spot of $d_\mathrm{L} = 12.8(19)\,\mu\mathrm{m}$ full-width at half-maximum (FWHM) is maintained at constant size. The energy on target is extrapolated from calibrations recorded at low-energy and the focal spot at high energy is estimated to be the same as for low-energy measurements. Note the large Rayleigh length of $464(145)\,\mu\mathrm{m}$ for this work, with

[1] Notation with the standard uncertainty in the last digits given in parenthesis in accordance with ISO GUM JCGM100:2008 7.2.2

https://doi.org/10.1017/hpl.2024.14 Published online by Cambridge University Press

a non-diffraction limited focal spot. For this experiment, $33.9(15)\,\%$ of the energy on target are within in the first Airy disk at low power. In addition there are three hot spots aside the focus in the first Airy ring, containing in total as much as $20(2)\,\%$ of the energy on target with an average intensity of $24(2)\,\%$ of the main intensity. The hot spots could not be optimized and might be due to the age of the parabola. The main peak intensity ranges from $2 \times 10^{19}\,\mathrm{W\,cm^{-2}}$ to $1.2 \times 10^{20}\,\mathrm{W\,cm^{-2}}$ and is the reference intensity for all calculations and plots in the following. The pulse duration is measured on-shot with a second-harmonic autocorrelator system that diagnoses the faint reflection from a thin pellicle positioned between parabola and focus.

The tape target system TaTaS-PW[30] transported aluminium tape of $10(1)\,\mu\mathrm{m}$ thickness, Kapton tape of $89(9)\,\mu\mathrm{m}$ thickness, tape of $10(1)\,\mu\mathrm{m}$ aluminium enforced with Kapton (Al-e-K)[30] and copper tape of $7(1)\,\mu\mathrm{m}$ thickness across the laser focal plane. Tapes are $12.5\,\mathrm{mm}$ wide stripes. The conductive $5\,\mathrm{mm}$ diameter support metal rods which guide the tape are $16\,\mathrm{mm}$ separated. Solid-density targets are placed in the laser focus position and tilted by $12.5°$ with respect to the laser axis to avoid reflection back towards laser amplifiers. As the VEGA laser pulse shows no pre-pulses capable of inducing a transparency or breakdown of the target[31], the main acceleration mechanism of charged particles is TNSA with the deployed laser and target parameters. In TNSA, a population of laser-heated forward-directed relativistic electrons escapes the target after crossing its thickness and the successive potential dynamics and electron-refluxing leads to the formation of sheath fields which are capable of accelerating ionized surface contaminants up to several tens of $\mathrm{MeV\,u^{-1}}$ [32]. The TCM measures the return current towards the target and allows us to deduce the total target charging by relativistic electrons. Note that the tape's only connection to the ground is one of the support metal rods. The other metal rod is floating with a total conductive length of $95\,\mathrm{mm}$. This forces the return current to flow thought the non-floating support metal rod and successively in the core of the coaxial transmission line that incorporates the TCM. The shield of the transmission line is grounded with the chassis of the tape target system.

Numerical simulations are performed to compare experimental results to theoretical predictions. The laser-driven target discharge is simulated with ChoCoLaT-2[16] (see Appx. B) - and the laser-absorption efficiency into hot electrons is studied with the particle-in-cell (PIC) code SMILEI[51] (see Appx. C).

3. Results and Discussion

We first show results from a single, representative shot on an aluminium target to emphasize different aspects of the platform, and secondly study the effect of changes of laser and target parameters based on single-shot data and high-repetition-rate recordings.

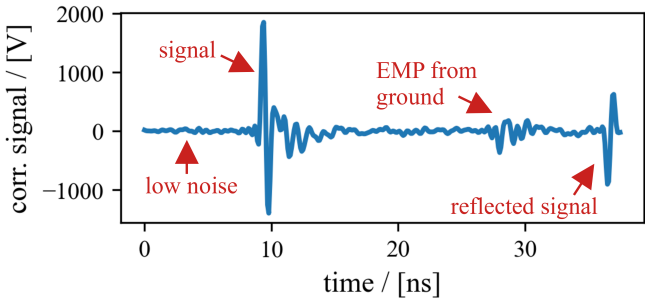

Figure 2. The circuit-corrected signal of the TCM for an aluminium target exhibits a clear positive peak for the rising edge of the positive current pulse. It is preceded by a low-noise pedestal; and followed by pulses streaming from the grounding to the target: first EMP induced noise and second the reflection of the current pulse at the impedance miss-matched ground. Time-base at TCM relative to laser-arrival at ≈0 ns.

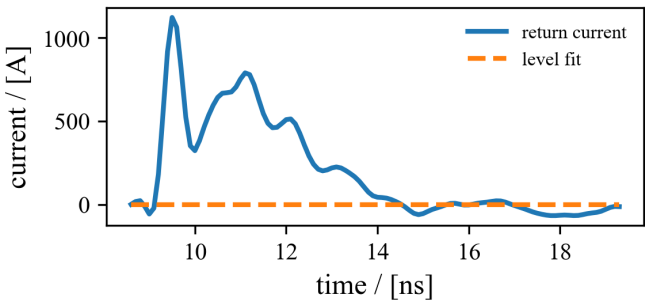

Figure 3. Current pulse (blue line) from an aluminium target retrieved by numerical integration from the derivative measured with the TCM. A first short primary peak is followed by a superposition of peaks in a broad secondary peak. Time-base relative to laser-arrival at ≈0 ns. The zero-level is controlled by comparison to a fit from before to after the current pulse (orange dashed line) – here in good agreement.

The inductive TCM device measures the derivative $\mathrm{d_t} I_\mathrm{p}$ of the pulsed current I_p streaming away from the target, see Fig. 2. Here, the laser pulse at $22.5\,\mathrm{J}$ beam energy (after compressor) and a duration of $30.4(7)\,\mathrm{fs}$ is fired onto a $10(1)\,\mu\mathrm{m}$ thick aluminium target. The laser impacts on the target at zero time seen from the TCM. The spatial distance between TCM and target is $30(1)\,\mathrm{cm}$ to ensure that the spherically expanding vacuum bound Electromagnetic Pulse (EMP) arrives at the device first. The EMP has no significant influence on the measurement as one does not notice noise in the pedestal leading to the signal. The signal exhibits a first positive peak that detects the rising edge of the current pulse streaming through the device. This indicates a positive current pulse propagating from the target to the ground. We measure the net negative charge escaping from the target – the time between electron and ion escape is too short to be resolved. The measurement shows also a reflection of the current pulse that streams back from the imperfectly impedance matched grounding towards the target; and EMP induced noise that couples into the transmission line when the spherically expanding EMP reaches the grounding.

After application of the instrument calibration, the

https://doi.org/10.1017/hpl.2024.14 Published online by Cambridge University Press

temporally-integrated signal is shown in Fig. 3. The peak amplitude reaches $1123(172)\,\mathrm{A}$. The FWHM τ_d of the narrow first peak is $400\,\mathrm{ps}$. A broad second peak follows and decays slowly towards zero, which is reached after $6\,\mathrm{ns}$. The first peak corresponds to the direct coupling of the discharge pulse into the transmission line to the TCM. The difference between the shortest (direct to ground) and longest way (to opposite end of rod) from the interaction region to the exit of the grounding rod is equivalent to $100\,\mathrm{ps}$ at the speed of light. Capacitive effects may broaden the peak further. The second peak most likely comprises multiple reflections across the conductive tape target.

Further temporal integration of ZI_p^2 yields the transported energy E_p and $\int I_\mathrm{p}\mathrm{d}t$ yields the transported charge Q_p. The total transported energy is $67(7)\,\mathrm{mJ}$. The energy conversion efficiencies from laser energy on target to current pulse energy results to $\chi_T = 0.4\,\%$; and the energy conversion efficiency only accounting for laser energy encircled in the laser focus and relativistic-intensity hot spots calculates to $\chi_S = 0.6\,\%$. The broad second peak contains a non-negligible fraction of the pulse energy in this configuration with $43(7)\,\mathrm{mJ}$. The temporally-resolved transported charge Q_p is shown in Fig. 4. The laser extracts $2.24(34)\,\mu\mathrm{C}$ from the target. The first peak of the current accounts for less than a third of the transported charge and the slow decay of the second peak allows the integral to reach a plateau only slowly.

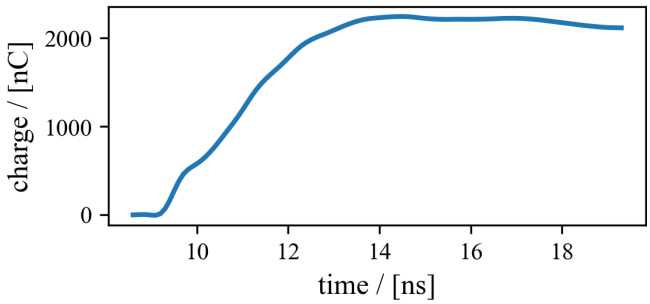

Figure 4. The transported charge from an aluminium target as obtained by numerical double-integration of the derivative measured by the TCM. The integral attains a plateau only slowly due to a slightly negative tail of the return current. Time-base relative to laser-arrival at ≈0 ns.

For a control of the accuracy of the numerical integrations, the zero-level is compared to a fit of both plateaus before and after the current pulse, shown as orange dashed line in Fig. 3. Here, the zero-level is maintained.

Crucial for applications, the current pulse is reproducible over hundreds of shots and is consistent with theoretical estimates. A current of $558(116)\,\mathrm{A}$ is obtained in 292 shots at $1\,\mathrm{Hz}$ for laser shots of $24.5(3)\,\mathrm{J}$ at $33(2)\,\mathrm{fs}$ onto copper tape of $7(1)\,\mu\mathrm{m}$ thickness. The average current and its standard deviation is shown in Fig. 5. The $8\,\%$ stability of the current measurement indicates a good shot-to-shot stability of laser and target parameters resulting in

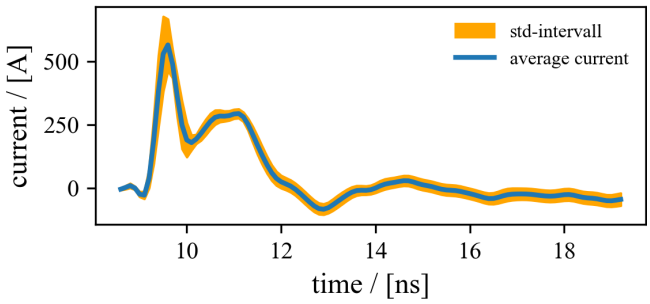

Figure 5. Average current and its standard deviation as obtained in 292 laser shots of $1.0(5)\times10^{20}\,\mathrm{W\,cm^{-2}}$ at 1 Hz onto copper tape. Time-base relative to laser-arrival at ≈0 ns. Multiple reflections across the conductive target yield a succession of multiple peaks.

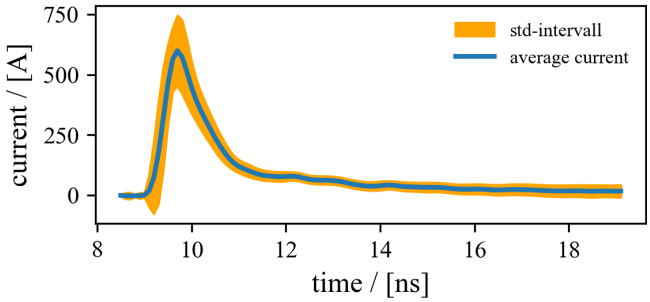

Figure 6. Average current and its standard deviation as obtained in 100 laser shots of $1.0(5)\times10^{20}\,\mathrm{W\,cm^{-2}}$ at $0.5\,\mathrm{Hz}$ onto Kapton tape. The dielectric target allows to produce single pulses. Time-base relative to laser-arrival at ≈0 ns.

a reproducible discharge dynamics and current production. The total transported charge amounts to $713(60)\,\mathrm{nC}$ and the current pulse energy is $11(2)\,\mathrm{mJ}$. The energy conversion efficiencies are lower compared to the ones for aluminium: $\chi_T^\mathrm{Cu} = 0.05\,\%$ and $\chi_S^\mathrm{Cu} = 0.09\,\%$.

ChoCoLaT-2 simulations predict $720(75)\,\mathrm{nC}$ of target discharge when assuming $68\,\%$ of the laser energy on target to be absorbed into electrons. Simulations take into account the experimental uncertainty for the pulse duration $(33(2)\,\mathrm{fs})$, $6.8(3)\,\mathrm{J}$ of laser energy within the first Airy disk and $4.1(3)\,\mathrm{J}$ distributed in three non-negligible hot spots with an average intensity of $24\,\%$ of the main intensity. The absorption efficiency into electrons is consistent with PIC simulations, see Appx. C. Such high values have been reported[34], depending on the presence of pre-plasma. If however the 2D PIC simulations should overestimate the absorption or no pre-plasma would be present, a typical[35,36] absorption of $50\,\%$ would still lead to an agreement with overlapping uncertainty intervals.

A comparison of the metallic targets above to a dielectric target reveals the likely influence of target reflections and shows how we can produce single-peak current pulses. A current of $597(153)\,\mathrm{A}$ is obtained in 100 shots at $0.5\,\mathrm{Hz}$ for laser shots of $22.9(2)\,\mathrm{J}$ at $33(1)\,\mathrm{fs}$ onto Kapton tape of $89(9)\,\mu\mathrm{m}$ thickness. The current evolution (averaged over

https://doi.org/10.1017/hpl.2024.14 Published online by Cambridge University Press

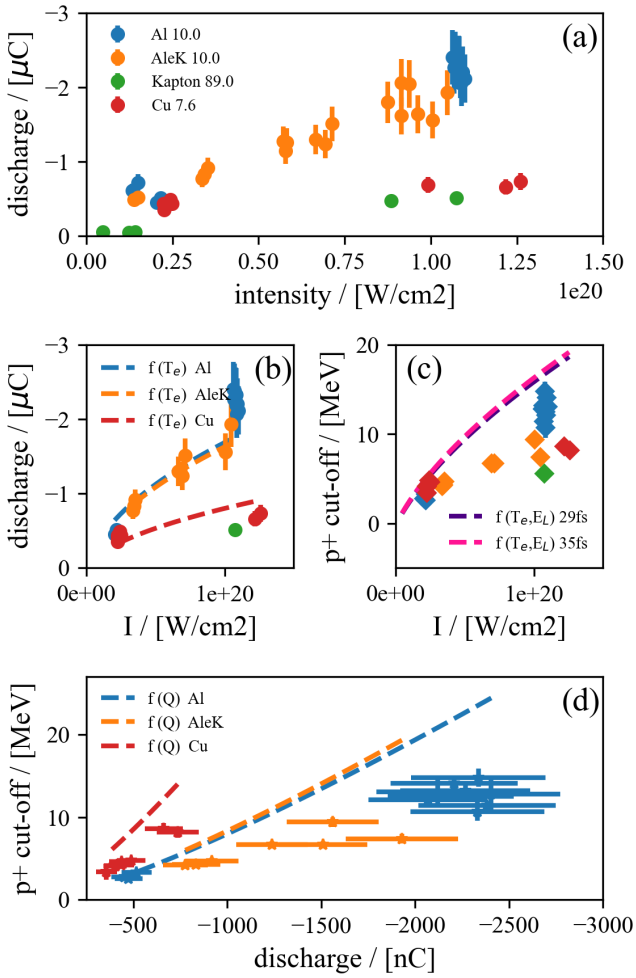

Figure 7. (a) Total charge measured under variation of laser pulse duration, energy, and the target material. (b–d) select data obtained at best laser compression. (b) Comparison with a semi-empirical model to derive the total charge from T_e and a material constant. (c) Spectral cut-off energies for protons in target-normal direction compared to available modelling [38], and (d) the relation between target charge and proton cut-off energy.

multiple shots) is shown in Fig. 6. The peak of 960 ps FWHM transports an average of 934(190) nC and has an energy of 13(4) mJ. The energy conversion efficiencies are comparable to the ones for copper: $\chi_T^{\mathrm{K}} = 0.06\,\%$ and $\chi_S^{\mathrm{K}} = 0.1\,\%$. In comparison to metallic targets, the primary peak is broadened due to a reduced conductivity and secondary peaks from reflections are missing. Multi-peak structures are indeed not expected to appear as reflections on tape ends do not occur, and reflections on other grounding stalks do not reach the signal transmission line with noticeable amplitude after the shot due to the low conductivity. Fewer reflections on the target may contribute towards the reduced EMP emission that is generally observed for dielectric targets [15].

Compared to the measurement for Kapton targets, simulations with ChoCoLaT-2 indicate a 10× lower current due to the dielectric nature of the material, but the code is not benchmarked for dielectric target materials where simulations do not consider the preplasma and preionization of the target material that will increase conductivity, lower the target potential and therefore increase the total target discharge.

It becomes clear that the current evolution and the amount of total charge varies considerably under variation of the target parameters. For a further parametric study on the variation of laser intensity, shots on aluminium tape, Kapton tape, tape of aluminium enforced with Kapton (Al-e-K) [30] and copper tape are compared in Fig. 7 (a). Most charge is ejected from aluminium targets, followed by copper and Kapton. Shots on aluminium reveal a monotonic relation between target discharge and intensity from $2.0\times10^{19}\,\mathrm{W\,cm^{-2}}$ to $1.2\times10^{20}\,\mathrm{W\,cm^{-2}}$. The large spread within the sets of data is due to the simultaneous variation of laser pulse duration and energy: when fixing the laser pulse energy, the ejected charge reaches a plateau towards shorter laser pulse duration consistent with available literature [16]. The platform allows for the production of tunable current pulses.

Fig. 7 (b) shows the amount of total charge under variation of the laser energy E_{L} for single-shot data obtained at best laser compression with a laser pulse duration ranging from 29 fs to 35 fs. The total target discharge can be modelled as a function of the hot electron temperature T_{e} of the laser-accelerated relativistic electron population as $Q_{\mathrm{p}} = A_{\mathrm{i}} \cdot T_{\mathrm{e}}$. Values for the tape dependent constant A_{i} are given in Tab. 1 which result from fits shown in Fig. 7 (b). Here T_{e} is presumed to follow the ponderomotive scaling [37]. One notes the good agreement of this square-root relation between laser energy and target discharge, which confirms previous work in the ponderomotive regime [16], and renders it possible to extrapolate the results to future experiments in similar conditions.

The thermalizing electron cloud is foundational to TNSA, which motivates a investigation of the relation between the return current and the sheath field based on properties of TNSA ions. The cut-off energy for TNSA-accelerated protons is obtained from a Thomson Parabola Ion Spectrometer [39] positioned towards the nominal target-normal direction, see Fig. 7 (c) for the same shots as in Fig. 7 (b). Fig. 7 (c) shows a proportionality between the proton cut-off energy and the total amount of charge.

The distribution of accelerated ions was successfully modelled in the regime relevant to this work [38], with the maximum energy of ions with charge Z scaling as $E_{\mathrm{i}}^{\mathrm{max}} = Z{\cdot}T_{\mathrm{e}}{\cdot}(P/T_{\mathrm{e}}-1)$, where P is a monotonically rising function of the maximum electron energy in the electron cloud. The

Table 1. Comparison of the proportionality factor A_{i} in the scaling model $Q_{\mathrm{p}} = A_{\mathrm{i}} \cdot T_{\mathrm{e}}$ for aluminium tape (Al), Kapton reinforced aluminium tape (AleK) and copper tape (Cu).

	Al	AleK	Cu
$A_{\mathrm{i}}/[\mathrm{nC\,MeV^{-1}}]$	538(45)	520(16)	256(26)

https://doi.org/10.1017/hpl.2024.14 Published online by Cambridge University Press

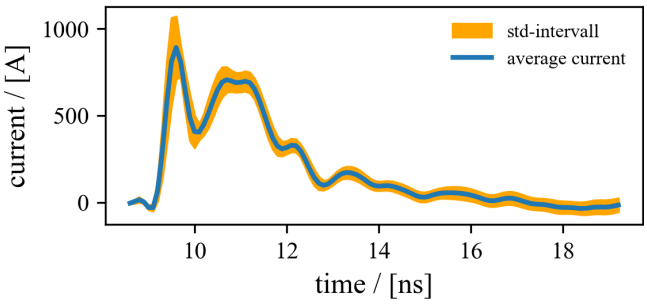

Figure 8. Average current and its standard deviation as obtained in 25 laser shots of $0.8(4) \times 10^{20}\,\mathrm{W\,cm^{-2}}$ at 1 Hz onto tape Al-e-K. Time-base relative to laser-arrival at ≈0 ns.

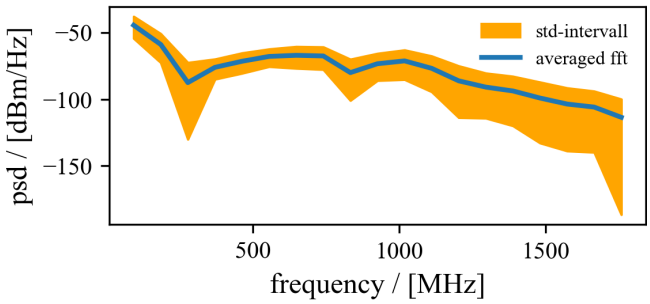

Figure 9. Average power spectrum density and its standard deviation as obtained in 25 laser shots of $0.8(4) \times 10^{20}\,\mathrm{W\,cm^{-2}}$ at 1 Hz onto tape Al-e-K. Time-base relative to laser-arrival at ≈0 ns.

ratio P/T_e simplifies to $P/T_\mathrm{e} \approx 4.8 + 0.8 \cdot \ln[E_\mathrm{L}^{[\mathrm{J}]}]$ for laser energies larger than several J[38]. The dashed lines in Fig. 7 (c) show the model predictions for each intensity at 29 fs and 35 fs. One notes that the model predictions are an upper bound for the measured proton cut-off energies. The model does not take into account material properties of targets and discrepancies might be due to differences in the accelerating potential induced by the respective size of the electron cloud that is influenced by electron scattering. Further, the model might be not applicable to Kapton targets as they are not conductive.

In order to relate target discharge and proton cut-off energy, both models are combined to deduce T_e from the total charge and calculate the proton cut-off energy accordingly. Respective predictions for each material are compared to the data as dashed lines in Fig. 7 (d). The agreement is fair when we consider the simplicity of the underlying models. There is a systematic overestimation by a factor of ≈ 1.8.

Note the geometry of tape Al-e-K: two 5 mm wide strips of 89 µm thick Kapton are glued on top of the aluminium tape at both its edges on the side facing the support metal rods. This Kapton reinforcement of aluminium is at mm-distance from the interaction zone, so it does not change the total amount of ejected charge (consistent with the experimental measurements in Fig. 7 (a)). However, in Fig. 7 (c) the proton cut-off energy in the spectrometer appears to be lower for tape Al-e-K than for aluminium tape. A tilt of the tape Al-e-K could have caused the proton cone to be not perfectly aligned towards the detector, resulting in a drop of detected maximum energy (as highest energies have smallest divergence in the TNSA scheme[9]). Such tilt are readily explained by tensions in the multi-layer structure. The temporal shape of the current pulse can however be influenced by the Kapton enforcement for tape Al-e-K, see Fig. 8 (compared to Fig. 3). The first peak is lower, which is consistent with the reduced coupling to the grounding due to the presence of Kapton at the tape edges. As a result the secondary peaks in the tail are elevated for reasons of more charge in reflections.

The characteristic parameters for all shot sequences are compared in Tab. 2. Current pulses from aluminium tape and reinforced aluminium tape are in a good agreement. Results for aluminium tapes exhibit higher current amplitudes when compared to copper targets due to a larger target discharge.

The bandwidth of the current pulse is large and allows for applications that require broadband pulses[26], see Fig. 9. Such pulses can be applied to steering antenna arrays or impulse radiating antennas to emit high power levels, i.e. in ground and subsurface radars for finding, recognition and reconstruction of moving objects.

4. Conclusions

We report the first generation and characterization of short pulsed kA-scale currents induced by high-power relativistic laser interaction at a high-repetition-rate. The pulses with several 100 ps FWHM show a <10 % stability in amplitude and a high energy conversion efficiency up to the order of 1 % from laser energy to pulse energy. Although the conversion efficiency of laser energy to electrical current can be one order of magnitude higher for kJ-class (ns-duration) laser pulses, fs-duration systems have the advantage of a high repetition rate and (potentially) more stable interaction conditions. Optimization of the energy conversion efficiency in relativistic interactions will be possible by optimizing the target discharge based on existing theoretical models[16], as the experimental data appears to agree well with simulations. Another advantage of the presented scheme is that it allows carrying the electrical impulse by cable out of the interaction chamber, whereas non-relativistically generated current dynamics clings to the close vicinity of the laser-target interaction point. Current pulses can be tailored by modifying the target: experimental data shows that the return current to metallic targets is broadened due to reflections across the target, whereas the use of dielectric targets removes those reflections leading to the generation of an overall shorter pulse peak.

The highest charge of 2.2(2) µC is produced with aluminium targets, followed by Kapton targets with 0.93(19) µC, and copper targets with 0.71(6) µC.

A direct application of such pulses can be the inductive

https://doi.org/10.1017/hpl.2024.14 Published online by Cambridge University Press

Table 2. Comparison of current pulses from shots on aluminium tape (Al), Kapton reinforced aluminium tape (AleK), Kapton tape (Kapton) and copper tape (Cu). Laser energy measured after compressor, N denotes the number of shots of the sequence, and χ_T is the ratio of energy confined in the current pulse to laser energy on target.

laser pulse				target			current pulse			
energy	duration	rate	N	tape	material	thickness	peak	charge	energy	χ_T
22.0(3) J	33(2) fs	0.5 Hz	87	Al	Al	10(1) µm	982(185) A	2.2(2) µC	58(9) mJ	0.32 %
21.9(3) J	37(4) fs	1 Hz	25	Alek	Al	10(1) µm	809(210) A	2.1(3) µC	45(8) mJ	0.25 %
22.9(2) J	33(2) fs	0.5 Hz	100	Kapton	Kapton	89(9) µm	597(153) A	0.93(19) µC	13(4) mJ	0.06 %
24.5(3) J	33(2) fs	1 Hz	292	Cu	Cu	7(1) µm	558(116) A	0.71(6) µC	11(2) mJ	0.05 %

generation of pulsed strong magnetic fields in small volumes. The pulse fills a solenoid if $\tau_\mathrm{d} \times c = 2\pi \times r_\mathrm{c} \times N_\mathrm{c}$, with the speed of light c, the radius of the coil r_c and N_c revolutions. Then the induced magnetic field in the coil centre attains $B_\mathrm{c} = \mu_0 I_\mathrm{d} c \tau_\mathrm{d} / 2\pi r_\mathrm{c} l_\mathrm{c}$, with vacuum permeability μ_0 and the length of the solenoid l_c. The measured pulse of 1.1 kA amplitude and 400 ps FWHM is apt for the generation of 11 T when using 1 mm diameter coils of 5 mm length, corresponding to 40 revolutions. Such magnetic fields can be used for the tailoring of MeV u^{-1} ions[20,21], i.e. laser-accelerated ion beams. They are also relevant for magnetization of secondary samples[40–42] if further temporally stretched, i.e. as seed fields in the context of magnetized implosions towards nuclear fusion.

Pulses of 1.1 kA in the 50 Ω circuit correspond to pulsed voltages of 55 kV, e.g. applicable to uni-polar nanosecond-pulse dielectric barrier discharge for producing non-thermal plasma at atmospheric pressure[43]; or the research of effects of ns and sub-ns pulses on biological cells[44–47].

Author Contributions

The author contributions are as follows: ME, IMV performed the data acquisition, curation and analysis; ME wrote the first draft of the manuscript; JC, PB, ME, TB commissioned the device at PALS; JLH organized the beamtime at CLPU; DL, RHM managed implementation of the device; ME, DL, JIA, RL contributed to conception and design of the study; all authors were involved with underlying experimental work; all authors contributed to manuscript improvement, read, and approved the submitted version.

Acknowledgements

This work would not have been possible without the help of the laser- and the engineering teams at CLPU and PALS. Special thanks for much appreciated support to the workshops of CLPU and PALS. This work received funding from the European Union's Horizon 2020 research and innovation program through the European IMPULSE project under grant agreement No 871161 and from LASERLAB-EUROPE V under grant agreement No 871124; as well as from the Grant Agency of the Czech Republic (Grant No. GM23-05027M); and Grant PDC2021-120933-I00 funded by MCIN/ AEI / 10.13039/501100011033 and by the "European Union NextGenerationEU/PRTR". The work was supported by funding from the Ministerio de Ciencia, Innovación y Universidades in Spain through ICTS Equipment grant No EQC2018-005230-P; further from grant PID2021-125389OA-I00 funded by MCIN / AEI / 10.13039/501100011033 / FEDER, UE and by "ERDF A way of making Europe" by the "European Union"; and in addition from grants of the Junta de Castilla y León with No CLP263P20 and No CLP087U16. This work has been carried out within the framework of the EUROfusion Consortium, funded by the European Union via the Euratom Research and Training Programme (Grant Agreement No. 101052200 — EUROfusion). Views and opinions expressed are however those of the author(s) only and do not necessarily reflect those of the European Union or the European Commission. Neither the European Union nor the European Commission can be held responsible for them. The involved teams have operated within the framework of the Enabling Research Projects: AWP17-ENR-IFE-CEA-02 *Towards a universal Stark-Zeeman code for spectroscopic diagnostics and for integration in transport codes* and AWP21-ENR-IFE.01.CEA *Advancing shock ignition for direct-drive inertial fusion*.

Data Availability Statement

The raw data and numerical methods that support the findings of this study are available from the corresponding author upon reasonable request.

A. TCM Calibration

A pulsed high voltage supply (500 ps FWHM) is used for the calibration of the Target Charging Monitor (TCM). The voltage supply is plugged to the top of the TCM. The through signal and the signal from the induced current are recorded on an oscilloscope of 20 GHz bandwidth using calibrated coaxial cables in a 50 Ω circuit, see Fig. 10. The current of the pulse can be naturally derived from the impedance of the circuit.

The induced signal is integrated numerically to derive the calibration factor between pulsed current and measured current, see Fig. 11. The numerical integration may lead to

https://doi.org/10.1017/hpl.2024.14 Published online by Cambridge University Press

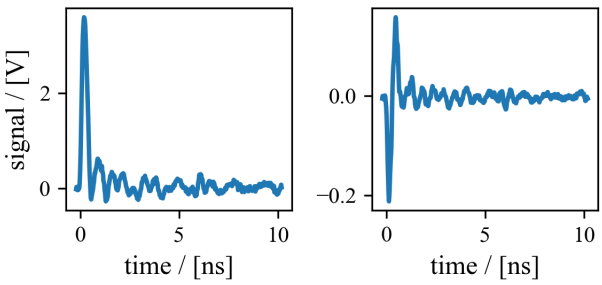

Figure 10. Through signal (left) and induced signal (right) corrected for attenuation of the respective circuit after the TCM.

what one observes as a change of the zero-level from before to after the peak. It is corrected for by fitting a zero-level with a linear regression. The difference between measurement and fit is fully taken into account in the following uncertainty estimates.

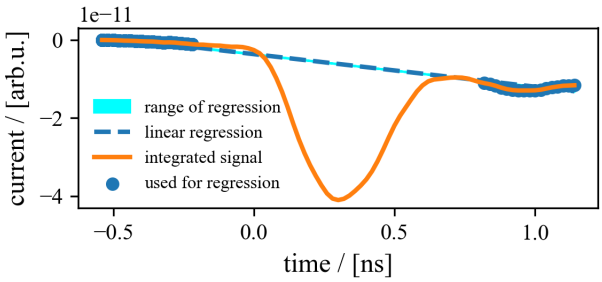

Figure 11. The integrated induced signal (orange line) shows a small offset after the pulse which might be due to numerical errors. Plateau regions before and after the peak are selected (blue dots) to fit a correction (dashed blue line) with respective uncertainty (cyan area).

The calibration factor which relates the integrated induced measurement in units of volt to the pulsed through current is obtained by fitting the base-corrected integrated induced signal to the through current, see Fig. 12. One obtains a calibration factor of $-2.0349(3117) \times 10^9\,\mathrm{A\,V^{-1}}$.

B. Discharge Simulations

The target discharge dynamics is studied using a detailed model of target charging in short laser pulse interactions[16] that predicts the expected discharge due to laser-heated relativistic electrons on a thin disk target. The initial electron distribution is based on laser parameters, with the temperature proportional to the intensity and the amount of charge proportional to the laser energy. The model takes into account the collisional cooling of electrons within cold solid density targets. Electrons are prevented from escaping the target by the target electric potential, which depends both on the target capacitance and the temperature of the plasma sheath at the target surface. The result of this calculations

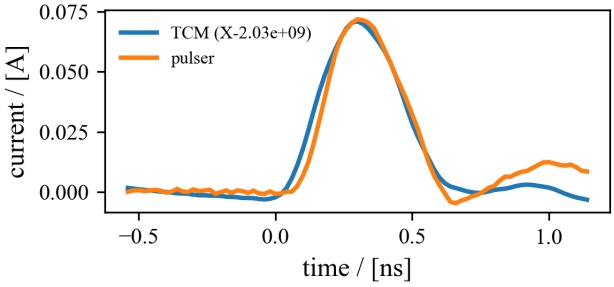

Figure 12. The integrated induced signal (blue line) is scaled to the pulsed through current (orange line) to obtain the calibration factor in units of $\mathrm{A\,V^{-1}}$.

is a total amount of target charge which can be compared to integrated measurements of return current.

The energy and time dependent hot electron distribution function $f(E,t)$ describes electrons inside the target and evolves according to

$$\partial_t f(E,t) = \frac{h_\mathrm{L}(E)\Theta(\tau_\mathrm{L}-t)}{\tau_\mathrm{L}} - \frac{f(E,t)}{\tau_\mathrm{ee}(E)} - g(E,t) \quad (1)$$

$$h_\mathrm{L}(E) \stackrel{!}{=} \frac{N_0}{T_0}\exp\left[-E/T_0\right] \quad (2)$$

$$N_0 \stackrel{!}{=} \int f(E,0)\,\mathrm{d}E \quad (3)$$

where $h_\mathrm{L}(E)$ is a constant exponential source of hot electrons, $\Theta(t)$ the Heaviside function limiting electron heating to the laser duration, $\tau_\mathrm{ee}(E)$ the energy dependent cooling time and $g(E,t)$ the rate of electron ejection from the target. The initial hot electron temperature T_0 depends on laser wavelength and pulse intensity[37,48,49]; and N_0 is re-normalized to the energy balance $N_0 T_0 = \eta E_\mathrm{L}$ between the total energy of hot electrons in the target and the absorbed laser energy. Simulations require the conversion efficiency η of laser energy to energy in the hot electron distribution, which is obtained by PIC simulations for this work (see Appx. C).

The hot electron cooling time depends on target material properties such as mass density ρ_t, mass number A_t, atomic number Z_t, and the hot electron energy distribution that allows to calculate average speed $\langle v\rangle_\mathrm{e}$ and energy $\langle E\rangle_\mathrm{e}$. Its meticulous calculation is demonstrated in[50] with an emphasis on cases relevant for this work.

With slight modifications to the source code, we can account for a second population of electrons produced by laser intensity hot-spots in and around the main focus. A section is added to construct an electron distribution based on the hot-spot energy and intensity, which then is added on top of the main electron distribution function.

https://doi.org/10.1017/hpl.2024.14 Published online by Cambridge University Press

C. PIC Simulations

The absorption of laser pulse energy into hot electron energy is studied for the case of shots on the copper target in a typical range of pre-plasma scale lengths. The absorption results to $61\,\%$ for $1\,\mu\mathrm{m}$ pre-plasma and $78\,\%$ for $3\,\mu\mathrm{m}$ pre-plasma. This range covers the absorption efficiencies required to reproduce experimental target charging by discharge simulations.

The 2D PIC simulation setup consists of a solid copper target irradiated by VEGA-3 laser system under an incidence angle of $12.5°$. The laser is linearly polarized and has the following characteristics: a wavelength λ of $800\,\mathrm{nm}$, a peak intensity of $7.5 \times 10^{19}\,\mathrm{W\,cm^{-2}}$ (corresponding to a normalized field amplitude $a_0 = 5.9$), a pulse duration of $33\,\mathrm{fs}$ FWHM and a transverse waist of $13\,\mu\mathrm{m}$. The copper target is considered fully ionized, having a density $100\ \mathrm{n_c}$, and a thickness of $7\,\mu\mathrm{m}$. The plasma density scale length is considered $1\,\mu\mathrm{m}$ and $3\,\mu\mathrm{m}$ for the two distinct simulations, having an exponential profile over a length of $20\,\mu\mathrm{m}$, and being ablated from the initial target thickness. The transverse width of the target is $40\,\mu\mathrm{m}$. At the rear side of the target we considered a thin layer of neutral protons of $70\,\mathrm{nm}$ thickness and $10\ \mathrm{n_c}$ density to simulate target contaminants. The simulation box has $80\,\mu\mathrm{m}$ in the longitudinal direction and $40\,\mu\mathrm{m}$ in the transverse direction. The cell length is $dx = dy = 12.5\,\mathrm{nm}$ and the number of particles per cell is 20 for each species. The particles are deleted while crossing the domain boundaries and the fields are absorbed. The simulations were performed with Simulating Matter Irradiated by Light at Extreme Intensities (SMILEI)[51] on the cluster Supercomputación Castilla y León (SCAYLE)[52].

References

1. T. H. Maiman et al., Stimulated Optical Radiation in Ruby, Nature 187 (1966), 493-494. https://doi.org/10.1038/187493a0
2. M. DiDomenico et al., Generation Of Ultrashort Optical Pulses by Mode Locking the YAIG:Nd Laser, Applied Physics Letters 8, 7 (1966), 180-183. https://doi.org/10.1063/1.1754544
3. P. Maine et al., Generation of ultrahigh peak power pulses by chirped pulse amplification, IEEE Journal of Quantum Electronics 24, 2 (1988) 398-403. https://doi.org/10.1109/3.137
4. M. Aoyama et al., 0.85 PW, 33 fs Ti:Sa laser, Optics Letters 28, 17 (2003), 1594-1596. https://doi.org/10.1364/OL.28.001594
5. T. Tajima and V. Malka, Laser plasma accelerators, Plasma Physics and Controlled Fusion 62, 034004 (2012). https://doi.org/10.1088/1361-6587/ab6da4
6. R. A. Snavely et al., Physical Review Letters **85**, 14 (2000). https://doi.org/10.1103/PhysRevLett.85.2945
7. S. C. Wilks et al., Phys. Plasmas **8**, 542 (2001). https://doi.org/10.1063/1.1333697
8. T. Esirkepov et al., Highly Efficient Relativistic-Ion Generation in the Laser-Piston Regime, Phys. Rev. Lett. 92, 17, 175003 (2004). https://doi.org/10.1103/PhysRevLett.92.175003
9. M. Borghesi, Ion Acceleration: TNSA and Beyond, Springer Proceedings in Physics 231 (2019). https://doi.org/10.1364/10.1007/978-3-030-25850-4_7
10. K. Nemoto et al., Laser-triggered ion acceleration and table top isotope production, Applied Physics Letters 78, 5 (2001) 595-597. https://doi.org/10.1063/1.1343845
11. M. I. K. Santala et al., Production of radioactive nuclides by energetic protons generated from intense laser-plasma interactions, Applied Physics Letters 78, 1 (2001) 19-21. https://doi.org/10.1063/1.1335849
12. F. E. Merrill et al., Proton Microscopy at FAIR, AIP Conference Proceedings 1195, 1 (2009) 667-670. https://doi.org/10.1063/1.3295228
13. F. Mirani et al., Integrated quantitative PIXE analysis and EDX spectroscopy using a laser-driven particle source, Science Advances 7, 3 (2021). https://doi.org/10.1126/sciadv.abc8660
14. M. Roth et al., Fast Ignition by Intense Laser-Accelerated Proton Beams, Physical Review Letters 86, 3 (2001) 436-439. https://doi.org/10.1103/PhysRevLett.86.436
15. F. Consoli et al., Laser produced electromagnetic pulses: generation, detection and mitigation, High Power Laser Science and Engineering 8, e22 (2020). https://doi.org/10.1017/hpl.2020.13
16. A. Poyé et al., Physical Review E 98, 033201 (2018). https://doi.org/10.1103/PhysRevE.98.033201
17. M. Ehret et al., Guided electromagnetic discharge pulses driven by short intense laser pulses: Characterization and modeling. Physics of Plasmas 30, 013105 (2023). https://doi.org/10.1063/5.0124011
18. P. Bradford et al., EMP control and characterization on high-power laser systems, High Power Laser Science and Engineering 6, e21 (2018). https://doi.org/10.1017/hpl.2018.21
19. J. L. Dubois et al., Experimental demonstration of an electromagnetic pulse mitigation concept for a laser driven proton source, Review of Scientific Instruments 89, 103301 (2018). https://doi.org/10.1063/1.5038652
20. S. Kar et al., Dynamic control of laser driven proton beams by exploiting selfgenerated, ultrashort electromagnetic pulses, Physics of Plasmas 23, 055711 (2016). https://doi.org/10.1063/1.4948725
21. M. Bardon et al., Physics of chromatic focusing, post-acceleration and bunching of laser-driven proton beams in helical coil targets, Plasma Physics and Controlled Fusion 62, 125019 (2020). https://doi.org/10.1088/1361-6587/abbe35

https://doi.org/10.1017/hpl.2024.14 Published online by Cambridge University Press

22. S. Fujioka et al., Sci. Rep. 3, 1170 (2013). https://doi.org/10.1038/srep01170
23. J. J. Santos et al., Physics of Plasmas 25, 056705 (2018). https://doi.org/10.1063/1.5018735
24. G. J. Williams et al., Laser intensity scaling of the magnetic field from a laser-driven coil target, J. Appl. Phys. 127, 083302 (2020). https://doi.org/10.1063/1.5117162
25. Y. Yan et al., Study of the time-domain electromagnetic pulse standard field generation setup and its application, Rev. Sci. Instrum. 89, 074703 (2018)
26. V. I. Koshelev et al., High-power ultrawideband electromagnetic pulse radiation, Proc. SPIE 3158, Intense Microwave Pulses V (1997). https://doi.org/10.1117/12.279432
27. S. -H. Min et al., Analysis of Electromagnetic Pulse Effects Under High-Power Microwave Sources, in IEEE Access 9, 136775-136791 (2021). https://doi.org/10.1109/ACCESS.2021.3117395.
28. K. H. Schoenbach et al., Bioelectric Effects of Intense Nanosecond Pulses, in IEEE Transactions on Dielectrics and Electrical Insulation 14, 5, 1088-1109 (2007). https://doi.org/10.1109/TDEI.2007.4339468.
29. A. Kiełbik, W. Szlasa, V. Novickij et al., Effects of high-frequency nanosecond pulses on prostate cancer cells, Sci Rep 11, 15835 (2021). https://doi.org/10.1038/s41598-021-95180-7
30. M. Ehret et al., High-repetition-rate solid tape target delivery system for intense laser-matter interactions, submitted (2023). https://doi.org/10.48550/arXiv.2302.04769
31. L. Volpe et al., High Power Laser Science and Engineering **7**, e25 (2019). https://doi.org/10.1017/hpl.2019.10
32. M. Roth and M. Schollmeier, Yellow Papers, CERN-2016-001 (2016). https://doi.org/10.5170/CERN-2016-001.231
33. J. Cikhardt et al., Measurement of the target current by inductive probe during laser interaction on terawatt laser system PALS, Review of Scientific Instruments 85, 103507 (2014). https://doi.org/10.1063/1.4898016
34. Y. Ping et al., Absorption of Short Laser Pulses on Solid Targets in the Ultrarelativistic Regime, Phys. Rev. Lett. 100, 8 085004 (2008). https://doi.org/10.1103/PhysRevLett.100.085004
35. J. Yu et al., Physics of Plasmas 6, 1318 (1999).
36. M. H. Key et al., Physics of Plasmas 5, 1966 (1998).
37. S. C. Wilks et al., Absorption of ultra-intense laser pulses, Physical Review Letters 69, 9 (1992) 1383-1386. https://doi.org/10.1103/PhysRevLett.69.1383
38. M. Passoni and M. Lontano, PRL 101, 115001 (2008).
39. Salgado-López et al., Proceedings of IBIC (2022). doi:10.18429/JACoW-IBIC2022-TU3C2
40. S. Sakata et al., Magnetized fast isochoric laser heating for efficient creation of ultra-high-energy-density states, Nature Communications 9, 3937 (2018). https://doi.org/10.1038/s41467-018-06173-6
41. G. Pérez-Callejo et al., Cylindrical implosion platform for the study of highly magnetized plasmas at Laser MegaJoule, Phys. Rev. E 106, 035206 (2022). https://doi.org/10.1103/PhysRevE.106.035206
42. C. A. Walsh et al., Exploring extreme magnetization phenomena in directly driven imploding cylindrical targets, Plasma Phys. Control. Fusion 64, 025007 (2022). https://doi.org/10.1088/1361-6587/ac3f25
43. S. Tao et al., Experimental study on repetitive unipolar nanosecond-pulse dielectric barrier discharge in air at atmospheric pressure, J. Phys. D: Appl. Phys. 41, 215203 (2008). http://dx.doi.org/10.1088/0022-3727/41/21/215203
44. J. M. Sanders et al., Scalable, Compact, Nanosecond Pulse Generator with a High Repetition Rate for Biomedical Applications Requiring Intense Electric Fields, 2009 IEEE Pulsed Power Conference, 11086266 (2009). https://doi.org/10.1109/PPC.2009.5386392
45. T. B. Naptonik et al., Effects of high voltage nanosecond electric pulses on eukaryotic cells (in vitro): A systematic review, Bioelectrochemistry 110, 1-12 (2016). https://doi.org/10.1016/j.bioelechem.2016.02.011
46. B. Greenebaum et al., Answers and questions: Forty years in bioelectromagnetics, Bioelectromagnetics 43:47-63 (2022). https://doi.org/10.1002/bem.22381
47. A. Porcher et al., Changesin Gene Expression After Exposing Arabidopsisthaliana Plantsto Nanosecond High Amplitude Electromagnetic Field Pulses, Bioelectromagnetics 00:1-12 (2023). https://doi.org/10.1002/bem.22475
48. R. Fabbro et al., Planar laser-driven ablation: Effect of inhibited electron thermal conduction, The Physics of Fluids 28, 5 (1985) 1463-1481. https://doi.org/10.1063/1.864982
49. F. N. Beg et al., A study of picosecond laser-solid interactions up to e19Wcm-2, Physics of Plasmas 4, 2 (1997) 447-457. https://doi.org/10.1063/1.872103
50. A. Poyé et al., Dynamic model of target charging by short laser pulse interactions, Physical Review E 92, 043107 (2015). http://dx.doi.org/10.1103/PhysRevE.92.043107
51. J. Derouillat et al., SMILEI: a collaborative, open-source, multi-purpose particle-in-cell code for plasma simulation Comput. Phys. Commun. 222 351–73 (2018). https://doi.org/10.1016/j.cpc.2017.09.024
52. Supercomputación Castilla y León (SCAYLE) (available at: https://www.scayle.es) (Accessed October 2023)

https://doi.org/10.1017/hpl.2024.14 Published online by Cambridge University Press